Simple and effective screening parameter for range-separated dielectric-dependent hybrids

Subrata Jana [1,*] Arghya Ghosh,[2] Lucian A. Constantin [3] and Prasanjit Samal[4]

[1]*Department of Chemistry and Biochemistry, The Ohio State University, Columbus, Ohio 43210, USA*
[2]*Department of Physics, Indian Institute of Technology, Hyderabad, India*
[3]*Istituto di Nanoscienze, Consiglio Nazionale delle Ricerche CNR-NANO, 41125 Modena, Italy*
[4]*School of Physical Sciences, National Institute of Science Education and Research, HBNI, Bhubaneswar 752050, India*

A simple effective screening parameter for the screened range-separated exchange-correlation hybrid functional is constructed from the compressibility sum rule, in the context of the linear-response time-dependent density functional theory. When applied to the dielectric-dependent hybrid (DDH), it becomes remarkably accurate for bulk solids, compared to those obtained from fitting with the model dielectric function or depending on the valence electron density of materials. The present construction of the screening parameter is simple and realistic. The screening parameter developed in this way is physically appealing and practically useful as it is straightforward to obtain using the average of the local Seitz radius over the unit-cell volume of the bulk solid. Furthermore, we have obtained a very good accuracy for energy band gaps, positions of the occupied d bands, ionization potentials, optical properties of semiconductors and insulators, and geometries of bulk solids (equilibrium lattice constants and bulk moduli) from the constructed DDH.

I. INTRODUCTION

Kohn-Sham (KS) density functional theory (DFT) [1,2] becomes the state-of-the-art method for the electronic structure calculations of solids and materials [3–9]. Although it is an exact theory, one must approximate the exchange-correlation (xc) part of the KS potential, which includes all the many-body interactions beyond the Hartree theory. The development of new xc approximations that have insightful physical content and which are also accurate as well as efficient for solids is always desirable [10–14]. In this respect, semilocal xc approximations [15–32] are quite useful because of their efficiency [33–46]. However, there are limitations when these semilocal xc functionals are applied to calculate band gaps for solids [35,47–53], optical spectrum [54–66], and semiconductor defects [67–71]. All these deficiencies of the semilocal xc functionals are related to the known delocalization error [47,72], which leads to the construction of hybrid functions with fractions of Hartree-Fock (HF) mixing [64,73–84]. Although the hybrid xc approximations of DFT solve many problems, they also have some limitations when a fixed HF mixing is used [55,67,85].

Nowadays, hybrid functionals with system-dependent HF mixing are fairly popular methods. Those are known as the dielectric-dependent hybrids (DDHs) [86–92], where the HF mixing is proportional to the inverse of the macroscopic static dielectric constant of the system under study. Such hybrids have been developed and applied to semiconductor and insulator bulk solids (but not for metals) for quite some time [93–100]. DDHs can be considered as the higher rung hybrids compared to those proposed from regular fixed HF mixing. Unlike hybrid functionals with fixed mixing parameters, in the case of DDHs, one needs to calculate the dielectric constant of the system beforehand. However, the great advantages of DDHs are that they are smartly constructed using the same philosophy as local Coulomb hole plus screened exchange (COH-SEX) [101] by fulfilling many important constraints that the exact xc functional must observe. Therefore, those possess similar accuracy as *GW* for band gaps and the Bethe-Salpeter equation (BSE) for optical spectra [55].

Regarding the several recently proposed DDHs, we recall range-separated DDH (RS-DDH) [88,89], DDH based on the Coulomb-attenuated method (DD-RSH-CAM) [90], and doubly screened DD hybrid (DSH) [91] based on their range separation. Also, there are other ways to implement the DDHs such as satisfaction of the Koopmans theorem [92]. A fairly good description and comparison of different versions of hybrids are discussed in Ref. [100]. Although the system-dependent macroscopic dielectric constant for DDHs is calculated from first principles [such as Perdew-Burke-Ernzerhof (PBE) or random-phase approximation (RPA) on the top of the PBE calculations (RPA-PBE)], the screening parameters are constructed from several philosophies, such as from the fitting of the long-wavelength limit of highly accurate dielectric functions [55,90,100] calculated from random-phase approximation (RPA) or nanoquanta kernel and partially self-consistent *GW* calculations [55,100], or from valence electron density [88,89,91,92]. Both are nonempirical choices and require no optimization procedure.

In this work, we propose an alternative procedure for obtaining the range-separated parameter for DDHs using a simple and effective way via the compressibility sum rule,

*subrata.niser@gmail.com

which connects the screening parameter with the exchange energy density. It is a quite realistic way of obtaining the screened parameter, where the relationship can be established through the linear-response time-dependent DFT (TD-DFT). Importantly, the present construction gives a very realistic result similar to those obtained from the model dielectric function. We assess the accuracy of screening parameters with DD-RSH-CAM [90] for the electronic properties of solids, especially band gaps, geometries, and optical properties.

The rest of the paper is organized as follows. Section II describes the generalized formulation of the range-separated DDH along with the construction of the screening parameter developed in this work. Section III presents results obtained from nonempirical screening parameters using the DD-RSH-CAM for solid properties. Section IV summarizes and concludes the work of this paper.

II. THEORY

A. The theoretical background of range-separated DDHs

We start from the Coulomb attenuated method (CAM)-style ansatz of the screened-range-separated hybrid (SRSH) functional by partitioning the Coulomb interaction as [102]

$$\frac{1}{r} = \frac{\alpha + \beta \, \text{erf}(\mu r)}{r} + \frac{1 - [\alpha + \beta \, \text{erf}(\mu r)]}{r}, \quad (1)$$

and the corresponding range-separated exchange-correlation (xc) functional becomes

$$
\begin{aligned}
E_{xc}^{\text{SRSH}} &= (1-\alpha)E_x^{\text{SR}-\text{SL},\mu} + \alpha E_x^{\text{SR}-\text{HF},\mu} \\
&\quad + [1-(\alpha+\beta)]E_x^{\text{LR}-\text{SL},\mu} + (\alpha+\beta)E_x^{\text{LR}-\text{HF},\mu} \\
&\quad + E_c^{\text{SL}}.
\end{aligned} \quad (2)
$$

Here, μ is the range-separation parameter. α and β control the fraction of short-range and long-range exchange to the above decomposition. In SRSH, the range separation is performed both on the Fock-like operator as well as semilocal exchange. In the present case, the semilocal (SL) short range (SR) and long range (LR) is based on the decomposition of the generalized gradient approximation (GGA) functional (PBE). However, meta-GGA semilocal functionals can also be used [78]. The aforementioned generalized decomposition can take several forms depending on the tuning of the α and β parameters. For example, (i) with $\beta = -\alpha$, the screened hybrid with SR-HF and LR-SL is recovered. This type of hybrid is useful for solids [64,73,77]. (ii) With the choice of $\alpha + \beta = 1$, in LR, the HF is always recovered [81,103]. This type of hybrid is useful for finite systems, especially for the long-range excitation of molecules [104]. And, finally, (iii) the global hybrid functional is obtained by considering $\beta = 0$ [105].

Though choice (i) is quite convenient for solids and popularly used in the name of Heyd-Scuseria-Ernzerhof (HSE) [73], it underestimates the band gaps of the insulators [52,90] and defect formation energies [67] because of the lack of dielectric screening. Considering these limitations, the SRSH hybrid has been constructed by incorporating the dielectric screening of solids as $\alpha + \beta = \epsilon_\infty^{-1}$, having the following expression:

$$
\begin{aligned}
E_{xc}^{\text{SRSH}} &= (1-\alpha)E_x^{\text{SR}-\text{SL},\mu} + \alpha E_x^{\text{SR}-\text{HF},\mu} \\
&\quad + \left(1-\epsilon_\infty^{-1}\right)E_x^{\text{LR}-\text{SL},\mu} + \epsilon_\infty^{-1}E_x^{\text{LR}-\text{HF},\mu} + E_c^{\text{SL}}, \quad (3)
\end{aligned}
$$

where ϵ_∞^{-1} is the inverse of the macroscopic static dielectric constant which is material specific. The main motivation of the underlying approximation is followed from Green's-function-based many-body approaches (GW exchange-correlation self-energy methods, Σ_{xc}), where the local Coulomb hole (COH) plus screened exchange (SEX) (COH-SEX) are taken into account. (See Ref. [91] for the connection between COH-SEX and DDHs.) The corresponding potential of the screened exchange is given as

$$
\begin{aligned}
V_{xc}^{\text{SRSH}}(\mathbf{r}, \mathbf{r}') &= \left[\alpha - \left(\alpha - \epsilon_\infty^{-1}\right)\text{erf}(\mu r)\right]V_x^{\text{Fock}}(\mathbf{r}, \mathbf{r}') \\
&\quad - \left(\alpha - \epsilon_\infty^{-1}\right)V_x^{\text{SR}-\text{SL},\mu}(\mathbf{r}) \\
&\quad + \left(1-\epsilon_\infty^{-1}\right)V_x^{\text{SL}}(\mathbf{r}) + V_c(\mathbf{r}), \quad (4)
\end{aligned}
$$

where $V_x^{\text{Fock}}(\mathbf{r}, \mathbf{r}')$ is the full-range Fock exchange,

$$V_x^{\text{Fock}}(\mathbf{r}, \mathbf{r}') = -\sum_{n\mathbf{k}} w_{\mathbf{k}} f_{n\mathbf{k}} \frac{\phi_{n\mathbf{k}}^{\text{KS}}(\mathbf{r}')\phi_{n\mathbf{k}}^{\text{KS}}(\mathbf{r})}{|\mathbf{r} - \mathbf{r}'|}, \quad (5)$$

with $\phi_{n\mathbf{k}}^{\text{KS}}(\mathbf{r})$ being the KS single-particle orbitals and $f_{n\mathbf{k}}$ their corresponding occupation numbers. Here, the sum is performed over all $\mathbf{k}$ points that sample the Brillouin zone (BZ) and n indicates the band indices at these $\mathbf{k}$ points with corresponding weights w_k. $V_x^{\text{SL}}(\mathbf{r})$ is the full-range semilocal functional (which is a PBE functional in the present case), $V_x^{\text{SR}-\text{SL},\mu}(\mathbf{r})$ is the short-range (SR) part of the PBE functional, and $V_c(\mathbf{r})$ is the PBE correlation. It may be noted that for solids, the reciprocal space representation of $\text{erf}(\mu r)$ becomes $e^{-|\mathbf{G}|^2/(4\mu)}$, where $\mathbf{G}$ is the reciprocal lattice vector. Several choices of the α, ϵ^{-1}, and μ exist and, based on those choices, rungs of screened exchange or DDH functionals may be constructed (see Ref. [100] for details).

In particular, we consider the case $\alpha = 1$, which is used in the doubly screened hybrid (DSH) [91] and the dielectric-dependent range-separated hybrid functional based on the Coulomb-attenuating method (CAM) (DD-RSH-CAM) [90], where the model dielectric function is defined as

$$\varepsilon^{-1}(\mathbf{G}) = 1 - \left(1-\epsilon_\infty^{-1}\right)e^{-|\mathbf{G}|^2/(4\mu)}. \quad (6)$$

However, the accuracy of Eq. (3) depends on two main aspects:

(i) The macroscopic static dielectric constant ϵ_∞^M is mostly calculated in a first-principles way using the linear-response TD-DFT method [106–108]. Also, dielectric constants calculated from RPA-PBE are reasonably well described [90]. For hybrids or DDHs, the dielectric constants are calculated using RPA + f_{xc}, where f_{xc} is the xc kernel [90,100]. Although there are several xc kernels (see Ref. [109] for a review), in the case of DD-RSH-CAM, the bootstrap approximation of Sharma *et al.* [60] ($f_{xc}^{\text{bootstrap}}$) is used [90].

(ii) The screening parameter μ is obtained following several procedures such as:

(a) from the fitting of the model dielectric function [Eq. (6)] with that of the long-wavelength limit of the diagonal elements of dielectric function i.e., $\varepsilon_{\mathbf{G},\mathbf{G}}^{-1}(\mathbf{q} \to 0, \omega = 0)$,

obtained from RPA calculations [90]. Thus, additional calculations within RPA (and/or a "nanoquanta" kernel combined with partially self-consistent GW) are required to obtain an accurate dielectric function [90]. We recall this screening parameter as $\mu = \mu_{\text{fit}}$ when used with DD-RSH-CAM and fitted from the model dielectric function of Eq. (6).

(b) The screening parameter μ can also be calculated from the valence electron density obtained for the range-separated dielectric-dependent hybrid (RS-DDH) [89]. In this case, μ is obtained from the Wigner-Seitz (WS) radius and Thomas-Fermi (TF) screening parameter as [89]

$$\text{RS} - \text{DDH}: \quad \mu = \mu_{\text{WS}} = \left(\frac{4\pi n_v}{3}\right)^{1/3}, \quad (7)$$

$$\mu = \mu_{\text{TF}} = \left(\frac{3 n_v}{\pi}\right)^{1/6}. \quad (8)$$

On the other hand, for DSH [91], the screening parameter is obtained as

$$\text{DSH}: \quad \mu = \mu_{\text{DSH}} = \frac{2}{3}\left(\frac{q_{\text{TF}}^2}{1.563\left(1 - \varepsilon_\infty^{-1}\right)}\right)^{1/2},$$

$$\text{where} \quad q_{\text{TF}}^2 = 4\left(\frac{3 n_v}{\pi}\right)^{1/3}. \quad (9)$$

Here, n_v is the valence electron density of the system under consideration [89,91].

(c) In Ref. [89], μ_{WS} and μ_{TF} are also obtained from the fitting of the long-range decay of the diagonal elements of the dielectric matrix calculated from the projective dielectric eigenpotential (PDEP) approach [89,110]. However, this fitting approach is similar to that of the method mentioned in (a). We also recall from Ref. [90] that $\mu = \mu_{\text{fit}}$ is also applied to RSH-DDH, where the fitting method mentioned in (a) is considered.

Alternatively, in the following, we propose a first-principles approach to construct the screening parameter μ from the linear-response TD-DFT.

B. A new formulation of the screening parameter

In the linear-response TD-DFT, the interacting $[\chi(\mathbf{r}, \mathbf{r}'; \omega)]$ and noninteracting $[\chi_0(\mathbf{r}, \mathbf{r}'; \omega)]$ density-density response functions are connected by the following Dyson-like equation [111]:

$$\chi(\mathbf{r}, \mathbf{r}'; \omega) = \chi_0(\mathbf{r}, \mathbf{r}'; \omega) + \int d\mathbf{r}_1 d\mathbf{r}_2 \, \chi_0(\mathbf{r}, \mathbf{r}_1; \omega)$$
$$\times v_{\text{eff}}[n](\mathbf{r}_1, \mathbf{r}_2; \omega)\chi(\mathbf{r}_2, \mathbf{r}'; \omega), \quad (10)$$

where

$$v_{\text{eff}}[n](\mathbf{r}, \mathbf{r}'; \omega) = \frac{1}{|\mathbf{r} - \mathbf{r}'|} + f_{xc}[n](\mathbf{r}, \mathbf{r}'; \omega) \quad (11)$$

is the Coulomb plus xc kernel known as the effective potential. If $f_{xc}[n](\mathbf{r}, \mathbf{r}'; \omega)$ is zero, then the RPA [112,113] is recovered. Therefore, $f_{xc}[n](\mathbf{r}, \mathbf{r}'; \omega)$ should account for the short-range correlation, which is missing in RPA. Following these considerations, Constantin and Pitarke (CP) proposed a simple and accurate approximation of $v_{\text{eff}}[n](\mathbf{r}, \mathbf{r}'; \omega)$ for the three-dimensional (3D) uniform electron gas (UEG), which is

given by [114,115]

$$v_{\text{eff}}^{\text{CP}}[n](\mathbf{r}, \mathbf{r}'; \omega) = \frac{\text{erf}(|\mathbf{r} - \mathbf{r}'|/\sqrt{4k_{n,\omega}})}{|\mathbf{r} - \mathbf{r}'|}. \quad (12)$$

Note that we already consider this type of splitting in the Coulomb interaction of DDH construction. Also, $4k_{n,\omega}$ is a frequency- and density-dependent function that controls the long-range effects of bare Coulomb interaction. Therefore, a direct connection between $4k_{n,\omega}$ and screening parameter μ can be established as follows:

$$\mu = \mu_{\text{eff}} = \frac{1}{\sqrt{4k_{n,\omega=0}}}. \quad (13)$$

Here, we denote μ_{eff} as the *effective* screening to distinguish it from the actual screening parameter used in the DD-RSH-CAM [90]. Note that for the DDH functionals of the ground-state DFT, we have to consider the static ($\omega = 0$) case.

The xc kernel for 3D UEG can be derived using the Fourier transform of Eqs. (11) and (12) as

$$f_{xc}(n; q, \omega) = \frac{4\pi}{q^2}\left[e^{-k_{n,\omega}q^2} - 1\right]. \quad (14)$$

Thus, in the long-wavelength ($q \to 0$) limit, one can obtain

$$k_{n,\omega} = -\frac{1}{4\pi} f_{xc}(n; q \to 0, \omega). \quad (15)$$

On the other hand, the long-wavelength limit of the static xc kernel $f_{xc}(n; q \to 0, \omega = 0)$ satisfies the compressibility sum rule [116],

$$f_{xc}(n; q \to 0, \omega = 0) = \frac{d^2}{dn^2}[n\epsilon_{xc}(n)], \quad (16)$$

where $\epsilon_{xc}(n)$ is the xc energy per particle of the 3D UEG. For $\epsilon_{xc}(n)$, we use the Perdew and Wang parametrization of the local density approximation (LDA) correlation energy per particle [117]. Note that the LDA xc kernel is remarkably accurate for $q < 2q_F$ ($q_F = (3\pi^2 n)^{1/3}$ is the Fermi wave vector), which explains the success of LDA (and semilocal functionals that recover LDA for the 3D UEG) for bulk solids [118,119].

Finally, Eqs. (15) and (16) give

$$k_{n,\omega=0} = -\frac{1}{4\pi}\frac{d^2}{dn^2}[n\epsilon_{xc}(n)], \quad (17)$$

and μ_{eff} can be found from Eq. (13). It is noteworthy that Eq. (13) is the central equation of this paper, which establishes a direct connection between the screening parameter and the LDA xc energy per particle [$\epsilon_{xc}(n)$] [117] that depends only on the local Seitz radius, $r_s = (\frac{3}{4\pi n})^{1/3}$, and the relative spin polarization, $\zeta = \frac{n_\uparrow - n_\downarrow}{n}$.

To simplify the computational implementation for bulk solids, we consider the average of r_s over the unit-cell volume, Ω_{cell}, as

$$\langle r_s \rangle = \frac{1}{\Omega_{\text{cell}}} \int_{\text{cell}} \left(\frac{3}{4\pi[n_\uparrow(\mathbf{r}') + n_\downarrow(\mathbf{r}')]}\right)^{1/3} d^3 r'. \quad (18)$$

We recall that this averaging technique over the unit cell has been considered earlier, e.g., in the construction of the modified Becke-Johnson (MBJ) semilocal exchange potential
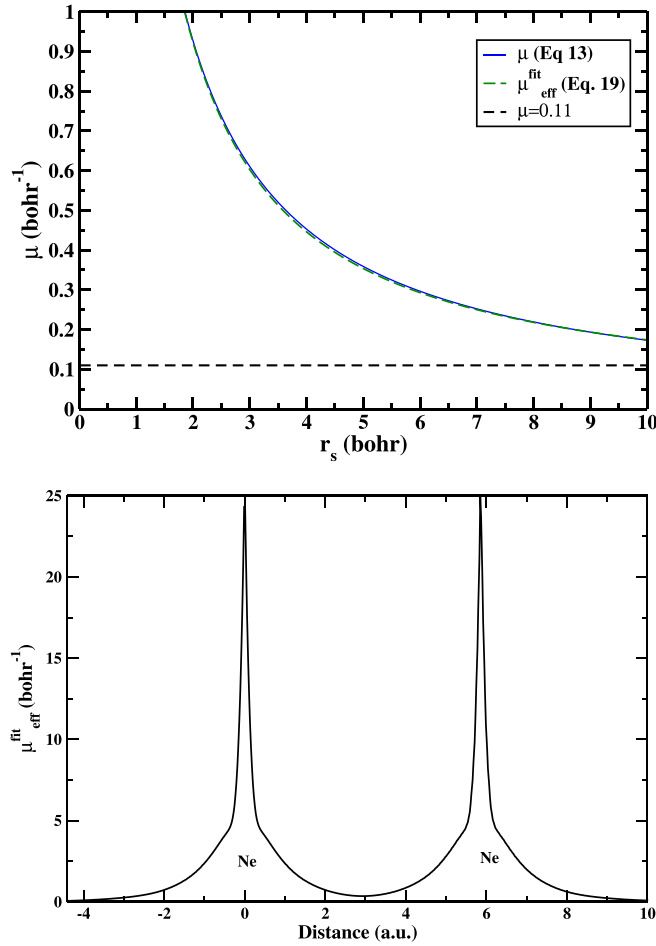
FIG. 1. Upper panel: The $\mu(r_s)$ as a function of local Seitz radius, r_s, for $0 < r_s < 10$ bohr. Lower panel: Range-separation function $\mu_{\text{eff}}^{\text{fit}}(\mathbf{r})$ for Ne_2, plotted as a function of the distance.

[49,120–124], local range-separated hybrid functionals [125], and xc kernel for optical properties of semiconductors [59]. For computational simplicity, we further fit the exact $\mu_{\text{eff}}(r_s)$ curve with the following formula (using the fact that $\mu \sim \frac{1}{r_s}$):

$$\mu_{\text{eff}}^{\text{fit}} = \frac{a_1}{\langle r_s \rangle} + \frac{a_2 \langle r_s \rangle}{1 + a_3 \langle r_s \rangle^2},\tag{19}$$

with $a_1 = 1.91718$, $a_2 = -0.02817$, and $a_3 = 0.14954$.

In Fig. 1 (upper panel), we plot $\mu(r_s)$ vs r_s for $0 < r_s < 10$ bohr. As one can see, $\mu_{\text{eff}}(r_s)$ and $\mu_{\text{eff}}^{\text{fit}}$ agree very well, with the curves being almost indistinguishable. We also observe that μ_{eff} is significantly bigger than the HSE one

($\mu^{HSE} = 0.11$), and only in the low-density regime ($r_s > 10$) do they become comparable. As a side note, $\mu_{\text{eff}}(r_s)$ also seems very realistic for long-range corrected (LC)-type hybrid functionals, where $\mu^{LC} \approx 0.50$ bohr^{-1} (see, for example, Table IV of Ref. [81]), because $\mu_{\text{eff}}(r_s) > 0.5$ bohr^{-1} for $r_s < 3.6$ bohr and $\mu_{\text{eff}}(r_s) < 0.50$ bohr^{-1} for $r_s > 3.6$ bohr.

The constructed $\mu_{\text{eff}}^{\text{fit}}(\mathbf{r})$ is also useful for hybrid functionals with local range separation [126]. In Fig. 1 (lower panel), we present a plot of our screening function, $\mu_{\text{eff}}^{\text{fit}}(\mathbf{r})$, for an Ne_2 dimer. As shown in Fig. 1, near the nucleus, $\mu_{\text{eff}}^{\text{fit}}(\mathbf{r})$ becomes high ($r_s \sim 0$), uniform at the middle of the bonds (r_s varies slowly), and zero at the tail ($r_s \to \infty$). To use this function as a local range-separated parameter, one may possibly use $\mu^{\text{local}}(\mathbf{r}) = \eta \mu_{\text{eff}}^{\text{fit}}(\mathbf{r})$, where η is an adjustable parameter ($0 < \eta < 1$).

In Table I, we compare different range-separated DDH methods along with different strategies for obtaining the screening parameter. One may note that all the methods proposed so far either depend on the valence electron density (n_v) or fitting the from dielectric function obtained using different higher-level methods. However, $\mu_{\text{eff}}^{\text{fit}}$, proposed here, can be obtained using $\langle r_s \rangle$ (or using the averaged density over the unit cell).

III. RESULTS

We combine $\mu_{\text{eff}}^{\text{fit}}$ with DD-RSH-CAM to obtain the properties of solids. Unless otherwise stated, DD-RSH-CAM denoted in this work is the original DDH presented in Ref. [90], whereas DD-RSH-CAM($\mu_{\text{eff}}^{\text{fit}}$) corresponds to the present work.

A. Screening parameter

We first calculate $\mu_{\text{eff}}^{\text{fit}}$ for several solids. We consider the same test set as considered in Ref. [90]. We use the all-electron code ELK [127], which uses linearized augmented plane waves (LAPWs) as a basis [128] to calculate $\mu_{\text{eff}}^{\text{fit}}$. The calculation of $\mu_{\text{eff}}^{\text{fit}}$ is performed using LDA densities with experimental lattice constants (given in Ref. [90]). Figure 2 compares μ and $\mu_{\text{eff}}^{\text{fit}}$ values for several solids, obtained from fitting with the model dielectric function and using the method described in this paper, respectively. When compared with μ, we observe $\mu_{\text{eff}}^{\text{fit}}$ deviates ~ 0.1 for all solids. For some solids such as BN, C, NiO, and SiC bulk solids, $\mu_{\text{eff}}^{\text{fit}}$ overestimates ~ 0.2. Figure 3 compares the model dielectric function as a function of reciprocal lattice vector $\mathbf{G}$. As observed from the relative mean-square error (RMSE), a maximum deviation of 0.060 is obtained for C, whereas we observe a very good

TABLE I. Comparison of different range-separated DDH functionals in terms of the Fock exchange fraction α and the range-separation parameter μ.

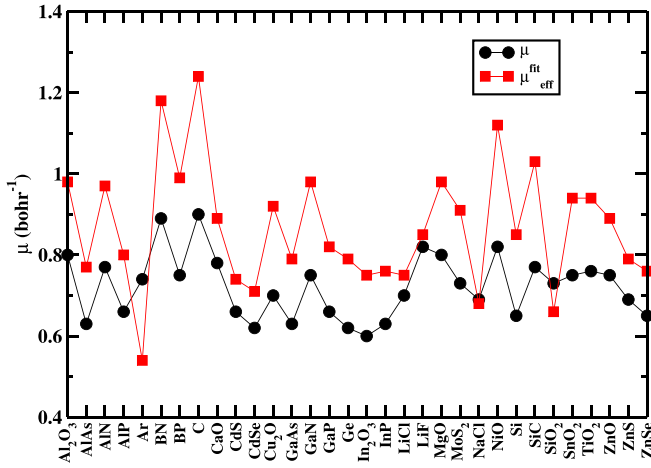| Methods	α of Eq. (4)	μ obtained from	Form of μ	μ fitted from model dielectric function	Ref.
RS-DDH	1/4	Eqs. (7) or (8)	$\mu_{\text{WS}}, \mu_{\text{TF}}$	No	Ref. [89]
		from fitting	$\mu_{\text{erfc-fit}}, \mu_{\text{TF-fit}}, \mu_{\text{fit}}$	Yes	Refs. [89,90]
DSH	1	Eq. (9)	μ_{DSH}	Yes	Ref. [91]
DD-RSH-CAM	1	from fitting of Eq. (6)	μ_{fit}	Yes	Ref. [90]
DD-RSH-CAM ($\mu_{\text{eff}}^{\text{fit}}$)	1	Eq. (19)	$\mu_{\text{eff}}^{\text{fit}}$	No	Present work

FIG. 2. The μ and μ_{eff}^{fit} for several solids reported in Table II. μ corresponds to the DD-RSH-CAM of Ref. [91] and μ_{eff}^{fit} is calculated in this work using Eq. (19).

agreement for MgO. The overall analysis of Figs. 2 and 3 suggests that the constructed μ_{eff}^{fit} from the compressibility sum rule agrees well with that of the μ obtained from the least-squares fitting of the model dielectric function.

Table II compares values of different screening parameters obtained using various strategies. As one can observe, in most cases, both μ_{WS} and μ_{TF} underestimate the values compared to μ. Here, the μ values are taken from Ref. [90] and supplied in the second column of Table II (we recall $\mu = \mu_{fit}$, as mentioned in Sec. II). However, as mentioned before, μ_{eff}^{fit} shows overestimation in most cases, when compared with μ fitted from the model dielectric function. One may note that calculations of μ_{eff}^{fit} can be done using LDA density (as done in this work) for the particular bulk solid before constructing ε_∞ self-consistently (not done in this work; rather, we have used values from Ref. [90]). This is possible as μ_{eff}^{fit} is not fitted from the model dielectric function, which also depends on

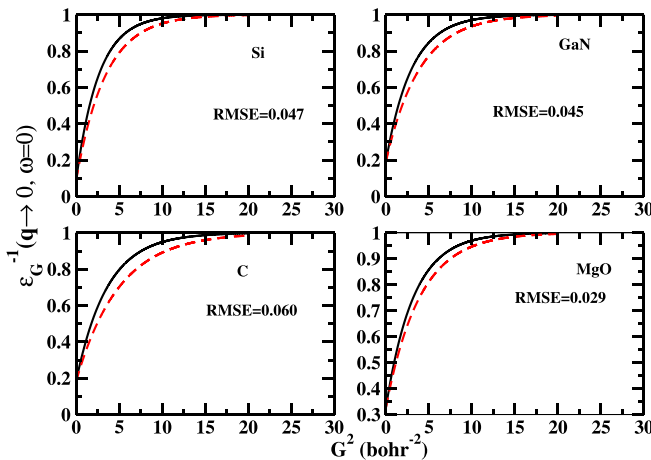FIG. 3. Comparison of model dielectric function as a function of **G** for four solids. Black solid line for the μ values of Ref. [90], whereas red dotted line for μ_{eff}^{fit}. Relative mean-square error (RMSE) of the model dielectric function as obtained from μ_{eff}^{fit} from the actual one (obtained using μ) is also shown.

TABLE II. Screening parameters μ (in bohr $^{-1}$) of the 32 semiconductors and insulators. For comparison, screening parameters obtained from other different methods are also shown.

Solids	μ^a	$\mu_{eff}^{fit\ b}$	μ_{WS}	μ_{TF}
Al$_2$O$_3$	0.80	0.98	0.71[c]	0.66[c]
AlAs	0.63	0.77	0.41[d]	0.50[d]
AlN	0.77	0.97	0.49[c]	0.55[c]
AlP	0.66	0.80	0.50[c]	0.55[c]
Ar	0.74	0.54	0.52[c]	0.56[c]
BN	0.89	1.18	0.75[c]	0.68[c]
BP	0.75	0.99	0.51[d]	0.56[d]
C	0.90	1.24	0.76[c]	0.68[c]
CaO	0.78	0.89	0.53[d]	0.57[d]
CdS	0.66	0.74	0.44[d]	0.52[d]
CdSe	0.62	0.71	0.42[d]	0.51[d]
Cu$_2$O	0.70	0.92	0.75[d]	0.68[d]
GaAs	0.63	0.79	0.41[d]	0.50[d]
GaN	0.75	0.98	0.60[c]	0.61[c]
GaP	0.66	0.82	0.43[d]	0.51[d]
Ge	0.62	0.79	0.45[d]	0.52[d]
In$_2$O$_3$	0.60	0.75	0.91[d]	0.74[d]
InP	0.63	0.76	0.39[d]	0.49[d]
LiCl	0.70	0.75	0.53[c]	0.57[c]
LiF	0.82	0.85	0.68[c]	0.64[c]
MgO	0.80	0.98	0.64[c]	0.63[c]
MoS$_2$	0.73	0.91	0.85[d]	0.72[d]
NaCl	0.69	0.68	0.49[c]	0.54[c]
NiO	0.82	1.12	0.82[c]	0.71[c]
Si	0.65	0.85	0.50[c]	0.55[c]
SiC	0.77	1.03	0.62[c]	0.62[c]
SiO$_2$	0.73	0.66	0.96[d]	0.76[d]
SnO$_2$	0.75	0.94	0.97[d]	0.77[d]
TiO$_2$	0.76	0.94	0.68[c]	0.65[c]
ZnO	0.75	0.89	0.78[c]	0.69[c]
ZnS	0.69	0.79	0.65[c]	0.63[c]
ZnSe	0.65	0.76	0.45[d]	0.52[d]
Arithmetic mean of μ	0.71	0.87	0.61	0.60

^{a}From Ref. [90] with DD-RSH-CAM level theory.
^{b}Present work using Eq. (19).
^{c}From Ref. [89].
^{d}Calculated in this work using Eqs. (7) and (8).

ε_∞. However, if μ is fitted from the model dielectric function, then one may also expect a self-consistent determination of $\mu = \mu_{fit}$ based on the output of ε_∞ (as the model dielectric function also depends on ε_∞).

B. Band gaps and valence band structures

Table III compiles the band gaps of 32 semiconductors and insulators using the static dielectric constants obtained from the DD-RSH-CAM (using the full expression including vertex corrections as mentioned in Ref. [90]). For all bulk band gaps, we use the plane-wave code Vienna *Ab initio* Simulation Package (VASP) [129–132], version 6.4.0. A Monkhorst-Pack (MP)-like $12 \times 12 \times 12$ Γ-centered **k** point is used for our calculations. For Al$_2$O$_3$ and In$_2$O$_3$, we reduce the **k** points to $8 \times 8 \times 8$. An energy cutoff of 550 eV is used for all our calculations. We use PBE pseudopotentials supplied with the VASP

TABLE III. The Kohn-Sham (KS) band gaps (in eV) as obtained using different methods. Band gaps of AlAs (0.11), GaAs (0.12), Ge (0.10), CdSe (0.14), and ZnSe (0.14) are corrected for spin-orbit coupling, as mentioned in Ref. [90]. Mean errors (MEs), mean absolute errors (MAEs), and mean absolute percentage errors (MAPEs) with respect to experimental results are also shown. Error statistics of RS-DDH(μ_{WS}) and RS-DDH(μ_{TF}) are calculated for 17 specified systems.

Solids	DD-RSH-CAM[a]	DD-RSH-CAM(μ_{eff}^{fit})[b]	RS-DDH(μ_{WS})[c]	RS-DDH(μ_{TF})[c]	Expt. [90]
Al_2O_3	9.51	9.56	9.63	9.61	9.10
AlAs	2.11	2.08			2.28
AlN	6.26	6.16	6.22	6.23	6.47
AlP	2.52	2.42	2.43	2.42	2.54
Ar	14.67	14.85	14.12	14.2	14.30
BN	6.56	6.39	6.33	6.34	6.74
BP	2.02	1.94			2.10
C	5.61	5.56	5.44	5.45	5.85
CaO	7.17	6.97			7.09
CdS	2.95	2.71			2.64
CdSe	1.75	1.76			1.88
Cu_2O	2.49	2.35			2.20
GaAs	1.45	1.27			1.57
GaN	3.50	3.42	3.30	3.3	3.68
GaP	2.42	2.25			2.43
Ge	0.50	0.54			0.79
In_2O_3	3.51	3.79			2.93
InP	1.55	1.35			1.47
LiCl	9.89	9.63	9.52	9.54	9.57
LiF	15.56	15.49	15.24	15.18	15.35
MgO	8.19	8.04	8.23	8.22	8.36
MoS_2	1.40	1.31			1.29
NaCl	9.10	8.79	8.60	8.66	9.14
NiO	4.68	4.44	4.45	4.51	4.30
Si	1.14	1.04	1.03	1.02	1.23
SiC	2.47	2.39	2.32	2.32	2.53
SiO_2	10.40	11.04			9.70
SnO_2	3.99	3.71			3.60
TiO_2	4.18	3.63	3.16	3.17	3.45
ZnO	3.74	3.73	3.75	3.67	3.60
ZnS	4.08	3.96	3.85	3.86	3.94
ZnSe	2.64	2.78			2.87
ME (eV)	0.09	0.01			
MAE (eV)	0.23	0.25			
MAPE	7.3	7.2			
ME (eV)[d]	0.09	−0.04	−0.15	−0.14	
MAE (eV)[d]	0.23	0.24	0.25	0.24	
MAPE[d]	4.5	4.6	5.3	5.2	

[a]From Ref. [90].

[b]Present work with ε_∞^{-1} calculated at DD-RSH-CAM level theory using RPA+$f_{xc}^{bootstrap}$. See Table IV of Ref. [90] for details.

[c]From Ref. [89].

[d]Calculated using 17 systems.

code to perform our calculations. In particular, for Ga, Ge, and In relatively deep, Ga 3d, Ge 3d, and In 4d pseudopotentials are used to treat valence orbitals. All band-gap calculations are performed with experimental lattice constants taken from Ref. [90].

The comparison of band gaps for different solids in Table III shows a fairly good agreement when calculations are performed using DD-RSH-CAM (μ_{eff}^{fit}). However, both panels of results for band gaps of Table III give an overall mean absolute error (MAE) ∼0.2 eV (MARE=7%) with respect to the experimental results. However, for a few solids, we observe that the DD-RSH-CAM (μ_{eff}^{fit}) results are a bit close

to that of the experimental values (such as for Cu_2O, In_2O_3, NiO, SnO_2, TiO_2, ZnS, and ZnSe). Regarding the RS-DDH method, it is also quite good in predicting the KS band gaps.

Finally, Fig. 4 compares the experimental vs calculated band gaps for DD-RSH-CAM and DD-RSH-CAM (μ_{eff}^{fit}). We observe that both methods perform similarly. Figure 4 also suggests that DD-RSH-CAM (μ_{eff}^{fit}) gives the slope of 1.03 (close to that of the DD-RSH-CAM) and an intercept of −0.14 eV, slightly larger than DD-RSH-CAM. These error statistics can also be compared with the other range-separated DDHs and HSE hybrid functional, as reported in Ref. [90]. We also recall from Ref. [90] that another range-separated
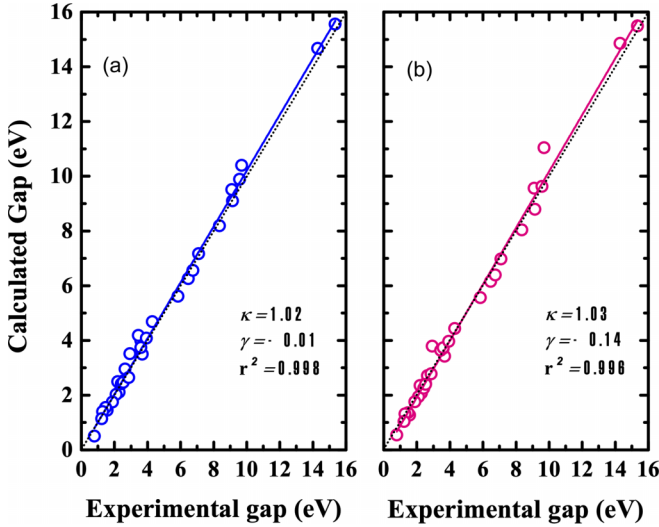
FIG. 4. The calculated vs experimental band gaps of 32 solids using (a) DD-RSH-CAM and (b) DD-RSH-CAM ($\mu_{\text{eff}}^{\text{fit}}$). See Table III for details of the computational procedures. The linear regressions formula that we have used in this work is given by $E_g^{\text{calc}} = \kappa E_g^{\text{expt}} + \gamma$, where κ is the slope, γ is the intercept (in eV), and r^2 is the correlation coefficient. $E_g^{\text{calc}} = E_g^{\text{expt}}$ is given by the dashed lines.

DDH, i.e., RS-DDH, gives an MAE = 0.37 eV and intercept of −0.33 eV for the same test set, which is much larger than both DD-RSH-CAM and DD-RSH-CAM ($\mu_{\text{eff}}^{\text{fit}}$). Overall, the performance of DD-RSH-CAM ($\mu_{\text{eff}}^{\text{fit}}$) suggests that this method performs as accurately as DD-RSH-CAM for band gaps of solids.

Next, we calculate the mean positions of the occupied d band of selective semiconductors, and the results are reported in Table IV. It is well known that approximate DFT xc functionals suffer from delocalization errors. Hence the average position of the occupied d state is underestimated, even for hybrids with fixed HF percentage. As shown in Ref. [90], DD-RSH-CAM can recover positions of the occupied d band correctly. A very similar performance is also observed from

Table IV for DD-RSH-CAM ($\mu_{\text{eff}}^{\text{fit}}$), which owns MAE of ∼0.4 eV, which is significantly close to that of higher-level methods such as $GW\Gamma^1$-HSE06 [101].

C. IPs and EAs

Another serious assessment of the DDHs is the determination of absolute band positions, hence ionization potentials (IPs) and electron affinities (EAs) calculated using the slab model [101,133–136]. As stated previously, due to the self-interaction error (SIE) (or delocalization error), semilocal functionals tend to underestimate relative band positions. Therefore, it is interesting to assess the performance of DD-RSH-CAM for extended systems, where the magnitude of the SIE strongly depends on the screening nature of the material under consideration. Here, we report IPs and EAs for II-VI and III-V semiconductors using DD-RSH-CAM ($\mu_{\text{eff}}^{\text{fit}}$).

Since a direct implementation of the DDHs to the slab model is not feasible because of computational cost, a more trivial way of doing this is to incorporate the corrections to the valance band maximum (VBM) state of the bulk system from DDHs, whereas the surface supercell slab calculations are performed using semilocal LDA/GGA approximations. In the present case, we use the Perdew-Burke-Ernzerhof (PBE) GGA functional. We recall that this method is similar to that of the quasiparticle (QP) GW-VBM approach as mentioned in Refs. [133,134]. Following the protocols of the GW-VBM method [133,134], the ionization potential at the DDHs level theory can also be defined as

$$\text{IP}^{\text{DDH}} = \text{IP}^{\text{SL}} - \Delta\varepsilon_{\text{VBM}}^{\text{DDH}}. \qquad (20)$$

Here, IP^{SL} is the IPs calculated in the semilocal level PBE-GGA functional as follows:

$$\text{IP}^{\text{SL}} = [\epsilon_{\text{Vac},s} - \epsilon_{\text{Ref},s}] - [\epsilon_{\text{VBM},b} - \epsilon_{\text{Ref},b}], \qquad (21)$$

and the corrections or shift to the VBM of the bulk solid because of DDH ($\Delta\varepsilon_{\text{VBM}}^{\text{DDH}}$) is given by

$$\Delta\varepsilon_{\text{VBM}}^{\text{DDH}} = \left[\epsilon_{\text{VBM},b}^{\text{DDH}} - \epsilon_{\text{Ref},b}^{\text{DDH}}\right] - [\epsilon_{\text{VBM},b} - \epsilon_{\text{Ref},b}]. \qquad (22)$$

TABLE IV. Mean positions of the occupied d band (in eV) relative to the VBM for selective semiconductors. The theoretical values are calculated by averaging the d state energies at the Γ point.

Solids	DD-RSH-CAM[a]	DD-RSH-CAM($\mu_{\text{eff}}^{\text{fit}}$)[b]	$GW\Gamma^1$-HSE06[c]	Expt.[d]
CdS	−9.7	−9.7	−9.5	−9.6
CdSe	−10.2	−10.0	−9.7	−10
InP	−17.3	−16.9	−16.9	−16.8
GaAs	−20.6	−19.8	−18.5	−18.9
GaN	−18.0	−17.7	−17.0	−17
GaP	−19.7	−19.4	−18.3	−18.7
ZnO	−7.5	−7.8	−7.1	−7.5
ZnS	−9.5	−9.4	−8.4	−9
ZnSe	−10.2	−9.8	−8.6	−9.2
MAE (eV)	0.7	0.4	0.3	

[a]From Ref. [90].
[b]Calculated using ε_∞^{-1} at DD-RSH-CAM level theory using RPA+$f_{xc}^{\text{bootstrap}}$. See Ref. [90] and Table for details.
[c]From Ref. [101].
[d]See Ref. [90] for experimental values.

TABLE V. Ionization potentials (IPs) and electron affinities (EAs) (where EA=IP-E_g in eV) of II-VI and III-V semiconductors as obtained from different methods. ME and MAE are calculated with respect to the experimental values. Spin-orbit effects are included as a correction in the theoretical bulk band gaps, as mentioned in Table III.

Solids	PBE		HSE06 [101]		DD-RSH-CAM[a]		DD-RSH-CAM (μ_{eff}^{fit})[b]		$GW\Gamma^1$-HSE06 [101]		Expt. [101]	
	IP	EA	IP	EA	IP	EA	IP	EA	IP	EA	IP	EA
AlAs	5.25	3.86	5.19	3.09	5.58	3.47	5.50	3.42	5.97	3.52	5.66	3.50
AlP	5.71	4.11	5.65	3.36	6.09	3.57	6.03	3.60	6.40	3.68	6.43	3.98
CdS	5.97	4.96	6.56	4.37	6.56	3.61	6.49	3.78	6.94	4.35	6.10	3.68
CdSe	5.60	5.24	6.06	4.48	6.01	4.26	5.92	4.16	6.62	4.71	6.62	4.50
GaAs	4.87	4.28	5.16	3.73	4.87	3.42	4.79	3.52	5.38	3.85	5.59	4.07
GaP	5.50	3.97	5.74	3.43	5.67	3.25	5.61	3.36	5.85	3.32	5.91	3.65
Ge	4.69	4.62	4.60	3.78	4.37	3.87	4.32	3.78	4.98	4.15	4.74	4.00
InP	5.15	4.74	5.60	4.10	5.14	3.59	5.08	3.72	5.74	4.16	5.77	4.35
Si	4.89	4.30	5.21	4.04	5.00	3.86	4.95	3.91	5.46	4.11	5.22	4.05
ZnS	6.09	4.11	6.74	3.42	7.16	3.08	7.06	3.10	7.18	3.29	7.50	3.90
ZnSe	5.61	4.61	6.15	3.71	6.47	3.83	6.36	3.59	6.71	3.79	6.79	4.09
MAE (eV)	0.63	0.46	0.42	0.33	0.39	0.36	0.45	0.36	0.21	0.28		
MAPE (%)	9.96	7.68	6.60	5.41	6.59	8.89	7.59	9.06	3.64	4.43		

[a]Calculated using ε_∞^{-1} and μ obtained from DD-RSH-CAM (see Ref. [90] for details).
[b]Calculated using ε_∞^{-1} obtained from DD-RSH-CAM and μ_{eff}^{fit}.

Here, $\epsilon_{\mathrm{Vac},s} - \epsilon_{\mathrm{Ref},s}$ is calculated for the surface supercell from semilocal functionals, which is PBE for the present case. For both the zinc-blende (zb) and diamond structures, we construct the nonpolar (001) surface supercell. $\epsilon_{\mathrm{Vac},s}$ and $\epsilon_{\mathrm{Ref},s}$ are the macroscopic average of the local electrostatic potential in the vacuum and the bulk region of the super-cell, respectively. From bulk calculations of semilocal and DDHs, $\epsilon_{\mathrm{VBM},b} - \epsilon_{\mathrm{Ref},b}$ and $\epsilon_{\mathrm{VBM},b}^{\mathrm{DDH}} - \epsilon_{\mathrm{Ref},b}^{\mathrm{DDH}}$ are determined, with $\epsilon_{\mathrm{VBM},b}$ (or $\epsilon_{\mathrm{VBM},b}^{\mathrm{DDH}}$) the position of the VBM in semilocal (or DDH) and $\epsilon_{\mathrm{Ref},b}$ ($\epsilon_{\mathrm{Ref},b}^{\mathrm{DDH}}$) the reference level for the bulk calculation for semilocal (or DDH), i.e., the average of the electrostatic potential in the unit cell.

In detail, we perform all bulk and surface calculations for IPs with the VASP code using the PBE-optimized geometries and ionic positions are relaxed further with Hellmann-Feynman forces of less than 0.005 eV/atom. To execute surface calculations, we first consider all nonpolar (001) surfaces including the Si and Ge diamond structures These slabs are made up of 14 atomic layers (18–39 Å) followed by 14 additional vacuum layers. All calculations (bulk and surface) are performed with a kinetic energy cutoff of 550 eV. The Γ-centered grid is used to sample the Brillouin zones (BZs), with $15\times15\times1$ **k** points for surface and $15\times15\times1$ **k** points for bulk calculations. As all the surfaces under consideration are nonpolar, we do not consider dipole corrections. The effect of spin-orbit coupling is evaluated for bulk calculations only since its inclusion in surface calculations has almost no influence on the electrostatic potential. One may note that the electrostatic potential used in this work is collected from the LOCPOT output file, which includes the sum of the ionic potential and the Hartree potential, not the exchange-correlation potential [137]. In this way, our PBE results match very well to that of the already reported PBE results in Ref. [101].

We show IPs and EAs of DD-RSH-CAM and DD-RSH-CAM ($\mu_{\mathrm{eff}}^{\mathrm{fit}}$) along with the HSE06 and $GW\Gamma^1$-HSE06 in Table V. For instance, we also plot, in Fig. 5, the VBM position (calculated from IPs and EAs) from DD-RSH-CAM ($\mu_{\mathrm{eff}}^{\mathrm{fit}}$) along with experimental IPs and EAs. As shown in Table V and Fig. 5, we observe that for II-VI and III-V semiconductors, IPs and EAs as obtained from both DDHs are well respected and have similar accuracy with the HSE06 ones. One may note that for II-VI and III-V solids, the performance of HSE06 is respectable [101], as those are medium-range band-gap solids and HSE06 describes well their screening. The similar accuracy of both DDHs indicates that these DDHs might also be a good choice for electronic structure calculations of semiconductors defects [67,92,138,139], where HSE06 with a fixed mixing parameter is not sufficient [67].

D. Optical absorption spectra

Hybrid functionals include nonlocal potential, which is the key for improving optical properties of bulk solids [54–58,145,147–150]. The optical absorption spectra as obtained from DDHs are realistic [144], including excitonic effects, i.e., $\sim \frac{\varepsilon_{\infty}^{-1}}{q^2}$ in the long-wavelength limit ($q \rightarrow 0$) [54,55]. The details of the methodology of the TD-DFT approach within DDH are given in Ref. [144]. Additionally, we also recall that several low-cost xc kernels are available
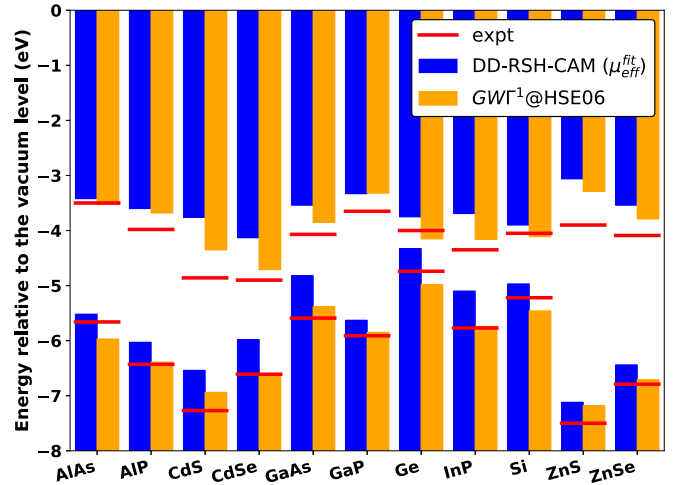

FIG. 5. Band alignments of II-VI and III-V semiconductors based on the IPs (negatives of the VBM to the vacuum level) and EAs (negatives of CBM to the vacuum level) as obtained from DD-RSH-CAM ($\mu_{\mathrm{eff}}^{\mathrm{fit}}$). For comparison, $GW\Gamma^1$-HSE06 [101] (shown by the bar) and experimental values (shown by a straight line) are also shown. All the surface orientations are along the (110) directions.

to compute the optical properties of semiconductors and insulators [59–63,151–153], describing well the excitons and excitonic effects (e.g., Bootstrap [60] and jellium-with-gap model (JGM) [59,151] kernels), in contrast to the RPA and adiabatic LDA (ALDA) kernels.

All calculations of DD-RSH-CAM ($\mu_{\mathrm{eff}}^{\mathrm{fit}}$) are performed by solving the Casida equation, as mentioned in Ref. [144]. To assess the performance of the DD-RSH-CAM ($\mu_{\mathrm{eff}}^{\mathrm{fit}}$), we calculate the imaginary [$\epsilon_2(\omega)$] and real [$\epsilon_1(\omega)$] parts of the macroscopic dielectric function ϵ^M of Si, C, MgO, and NaCl in the optical limit of small wave vectors,

$$\epsilon_2(\omega) = \mathrm{Im}\left\{\lim_{q \rightarrow 0} \epsilon^M(q, \omega)\right\},$$

$$\epsilon_1(\omega) = \mathrm{Re}\left\{\lim_{q \rightarrow 0} \epsilon^M(q, \omega)\right\}. \quad (23)$$

We recall that the optical absorption spectrum is given by $\epsilon_2(\omega)$, while other optical properties (e.g., Fresnel reflectivity at normal incidence, and the long-wavelength limit of the electron-energy-loss function) depend on both $\epsilon_1(\omega)$ and $\epsilon_2(\omega)$.

For the optical absorption spectrum, we use the VASP code with $32\times32\times32$ MP-like **k** points and 20 empty orbitals. Since a straightforward calculation of DDH using these dense **k** points would be expensive, we have performed the DDH calculations in many shifted $8\times8\times8$ grids (i.e., $8\times8\times8$ **k**-point grid and shifted with 0.25 irreducible **k** points [154]) and then averaged over respective weights or multiple grids, as mentioned in Ref. [154]. All calculations are performed with experimental lattice constants. We use complex shift (CSHIFT) 0.3 to smoothen the real part of the dielectric function in all our calculations.

For the Si bulk, we observe quite realistic absorption spectra from DD-RSH-CAM ($\mu_{\mathrm{eff}}^{\mathrm{fit}}$), showing two excitation peaks at the right positions corresponding to the experimental results. However, the first peak at ~ 3.5 eV, which represents
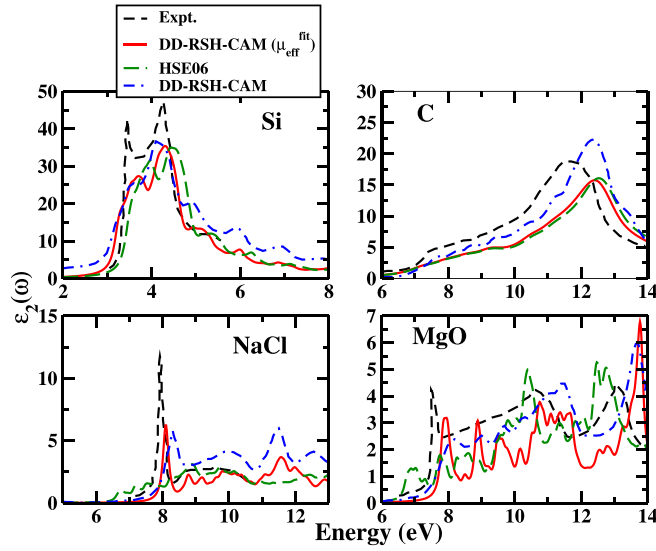
FIG. 6. Imaginary part of absorption spectra $[\epsilon_2(\omega)]$ of Si, C, NaCl, and MgO, calculated with DD-RSH-CAM ($\mu_{\rm eff}^{\rm fit}$), HSE06, and DD-RSH-CAM functionals. Experimental spectra are taken from Ref. [140] (for Si), Ref. [141] (for C), Ref. [142] (for NaCl), and Ref. [143] (for MgO). Calculations of DD-RSH-CAM ($\mu_{\rm eff}^{\rm fit}$) are performed using DD-RSH-CAM's ε_∞^{-1}. Absorption spectra of DD-RSH-CAM are taken from Ref. [144].
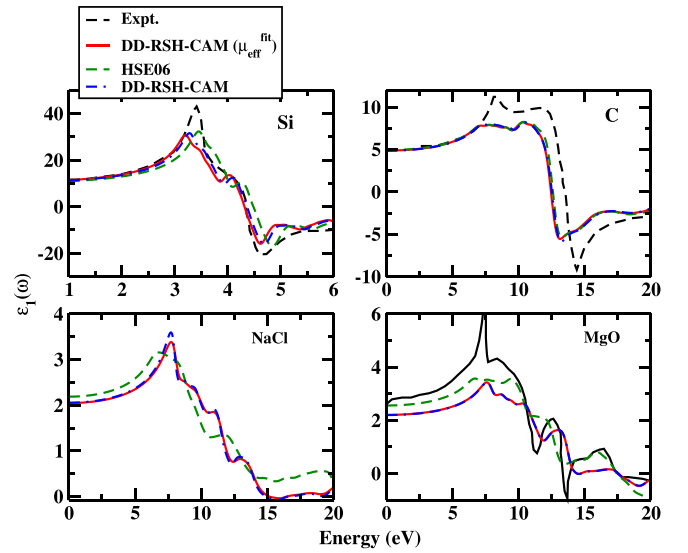
FIG. 7. Real part of absorption spectra $[\epsilon_1(\omega)]$ for Si, C, and MgO calculated with DD-RSH-CAM ($\mu_{\rm eff}^{\rm fit}$), HSE06, and DD-RSH-CAM functionals. The Si and C experimental data are taken from Ref. [145], and the MgO experimental data are from Ref. [146]. Calculations of DD-RSH-CAM ($\mu_{\rm eff}^{\rm fit}$) are performed using DD-RSH-CAM's ε_∞^{-1}.

the oscillator strength, is always underestimated, similar to the hybrids with fixed mixing parameters. A similar performance is also observed for DD-RSH-CAM, as shown in Ref. [144]. Next, considering the optical spectra of the medium gap semiconductor C diamond, the DD-RSH-CAM ($\mu_{\rm eff}^{\rm fit}$) peak is blueshifted with about 1 eV because of the slightly larger value of $\mu_{\rm eff}^{\rm fit}$ (see Fig. 2). However, we obtain reasonable

absorption spectra of NaCl and MgO insulators, which are considered difficult tests for all the computational methods. Compared to the absorption spectra of DD-RSH-CAM, as studied in Ref. [144], we see similar tendencies from the present method. One may also note from Fig. 6 that for the wide band-gap insulators, the performance of HSE06 is unsatisfactory, underestimating the absorption peak.

TABLE VI. Lattice constant (a_0) and bulk modulus (B_0) for selective solids. Mean percentage errors (MPEs) and mean absolute percentage errors (MAPEs) of lattice constants and bulk moduli are also given.

Solids	a_0 (Å)			B_0 (GPa)		
	DD-RSH-CAM[a]	DD-RSH-CAM($\mu_{\rm eff}^{\rm fit}$)[b]	Expt.[c]	DD-RSH-CAM[a]	DD-RSH-CAM($\mu_{\rm eff}^{\rm fit}$)[b]	Expt.[d]
BN	3.584	3.592	3.594	410	400	400
BP	4.527	4.531	4.527	172	165	173
C	3.552	3.551	3.555	438	455	442
CaO	4.755	4.77	4.781	124	121	120
GaAs	5.718	5.657	5.641	71	72	77
Ge	5.719	5.679	5.644	69	68	76
LiCl	5.092	5.068	5.072	33	35	35
LiF	3.927	3.92	3.974	82	86	70
MgO	4.158	4.148	4.188	179	183	165
NaCl	5.594	5.554	5.565	26	27	27
Si	5.447	5.444	5.422	96	95	99
SiC	4.349	4.352	4.348	229	230	225
MPE (%)	0.1	−0.1		0.2	1.3	
MAPE (%)	0.6	0.4		5.3	5.6	

[a]From Ref. [90].

[b]Calculated using ε_∞^{-1} obtained from DD-RSH-CAM and $\mu_{\rm eff}^{\rm fit}$.

[c]See Table VIII of Ref. [90] for details of the reference values. The zero-point anharmonic expansion (ZPAE) is included in the experimental lattice constants.

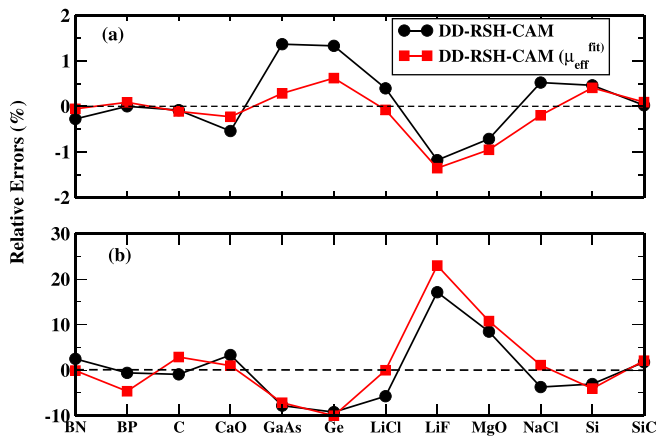[d]See Table VIII of Ref. [90] for the references of bulk moduli.

FIG. 8. DD-RSH-CAM and DD-RSH-CAM (μ_{eff}^{fit}) relative errors (in %) for the (a) equilibrium lattice constants and (b) bulk moduli of several bulk solids. The DD-RSH-CAM results are from Ref. [90].

Furthermore, in Fig. 7, we show the real part of the dielectric function. In the cases of Si and C, both the TD-DFT spectra of DD-RSH-CAM (μ_{eff}^{fit}) and HSE06 are in excellent agreement with the experimental data. However, for the NaCl and MgO insulators, DD-RSH-CAM (μ_{eff}^{fit}) is more realistic and the peaks are in the correct positions. One may also note that both the real and imaginary parts of DD-RSH-CAM match quite well with that of DD-RSH-CAM (μ_{eff}^{fit}), especially the peak position. For the imaginary part of DD-RSH-CAM, we consider results from Ref. [144], whereas we calculate DD-RSH-CAM for the real part.

E. Structural properties

Structural properties of DDH are performed using VASP with a similar setup as mentioned in Sec. III B. In Table VI, we calculate the structural properties of selective solids compiled in Ref. [90]. We obtain very reasonable equilibrium lattice constants and bulk moduli for a wide range of solids using DD-RSH-CAM (μ_{eff}^{fit}). For lattice constants, the overall MAPE of 12 solids is obtained to be 0.4%, slightly better than DD-RSH-CAM. For bulk moduli, both perform similarly with MAPE ~5%. In Fig. 8, we plot the percentage error of lattice constants and bulk moduli for 12 solids using the two DDHs. We observe that DD-RSH-CAM (μ_{eff}^{fit}) improves over DD-RSH-CAM for the lattice constants of most solids.

For bulk moduli, the overall MAPE is within 6% for both DDHs. Reference [90] also suggests that HSE06 offers similar accuracy as DD-RSH-CAM for both lattice constants and bulk moduli. Hence, a good description of the structural properties can be acquired from DD-RSH-CAM (μ_{eff}^{fit}) across a wide variety of materials.

One may also note that from the trends shown in Tables III–VI, the results of both DDHs are more sensitive to the choice of macroscopic static dielectric constant than to the inverse screening length μ. Hence, one can simply choose its mean value, such as 0.7 bohr^{-1} or 0.8 bohr^{-1} (see the last line of Table II), which is material independent. However, for more accurate calculations, one has to carefully consider both the macroscopic static dielectric constant and the material-dependent inverse screening length. Hence, the present procedure should be quite useful, as one can obtain μ entirely from first principles.

IV. CONCLUSIONS

We have presented a simple and effective way to determine the screening parameter for dielectric-dependent hybrids from the compressibility sum rule combined with the linear-response time-dependent density functional theory. When applied to the bulk solids, the resultant effective screening parameter, named μ_{eff}^{fit}, performs with similar accuracy for bulk solids as that obtained from the fitting with (model) dielectric function or valence electron density. Importantly, the present effective screening parameter depends only on the local Seitz radius, which is averaged over the unit-cell volume of the solid, having no fitted empirical parameters. In particular, the main advantage of the present procedure is that it does not depend on the dielectric function and it can be obtained entirely from first-principles calculations for any bulk system.

Finally, our calculations show that DD-RSH-CAM (μ_{eff}^{fit}) shows similar accuracy as DD-RSH-CAM for band gaps, positions of the occupied d bands, and ionization potentials. Also, it is quite successful for semiconductor and insulator optical properties as well as for the structural properties of solids. Importantly, one can obtain the value of μ_{eff}^{fit} quite easily for any bulk solids, which we believe in turn reduces the computational difficulty. For example, one can obtain the macroscopic static dielectric constants from PBE (using density functional perturbation theory [155,156]) and combine them with μ_{eff}^{fit} to perform calculations for materials.

[1] W. Kohn and L. J. Sham, Phys. Rev. **140**, A1133 (1965).

[2] P. Hohenberg and W. Kohn, Phys. Rev. **136**, B864 (1964).

[3] K. Burke, J. Chem. Phys. **136**, 150901 (2012).

[4] E. Engel and R. M. Dreizler, *Density Functional Theory* (Springer, New York, 2013).

[5] R. O. Jones, Rev. Mod. Phys. **87**, 897 (2015).

[6] A. J. Cohen, P. Mori-Sánchez, and W. Yang, Chem. Rev. **112**, 289 (2012).

[7] P. J. Hasnip, K. Refson, M. I. J. Probert, J. R. Yates, S. J. Clark, and C. J. Pickard, Philos. Trans. R. Soc. A **372**, 20130270 (2014).

[8] S. Kümmel and L. Kronik, Rev. Mod. Phys. **80**, 3 (2008).

[9] A. M. Teale, T. Helgaker, A. Savin, C. Adamo, B. Aradi, A. V. Arbuznikov, P. W. Ayers, E. J. Baerends, V. Barone, P. Calaminici, E. Cancès, E. A. Carter, P. K. Chattaraj, H. Chermette, I. Ciofini, T. D. Crawford, F. De Proft, J. F. Dobson, C. Draxl, T. Frauenheim *et al.*, Phys. Chem. Chem. Phys. **24**, 28700 (2022).

[10] J. P. Perdew and K. Schmidt, AIP Conf. Proc. **577**, 1 (2001).

[11] G. E. Scuseria and V. N. Staroverov, in *Theory and Application of Computational Chemistry: The First 40 Years*, edited by

C. E. Dykstra, G. Frenking, K. S. Kim, and G. E. Scuseria (Elsevier, Amsterdam, 2005), pp. 669–724.

[12] F. Della Sala, E. Fabiano, and L. A. Constantin, Intl. J. Quantum Chem. **116**, 1641 (2016).

[13] J. P. Perdew, V. N. Staroverov, J. Tao, and G. E. Scuseria, Phys. Rev. A **78**, 052513 (2008).

[14] J. P. Perdew, A. Ruzsinszky, J. Tao, V. N. Staroverov, G. E. Scuseria, and G. I. Csonka, J. Chem. Phys. **123**, 062201 (2005).

[15] J. P. Perdew, K. Burke, and M. Ernzerhof, Phys. Rev. Lett. **77**, 3865 (1996).

[16] J. P. Perdew, A. Ruzsinszky, G. I. Csonka, O. A. Vydrov, G. E. Scuseria, L. A. Constantin, X. Zhou, and K. Burke, Phys. Rev. Lett. **100**, 136406 (2008).

[17] C. Lee, W. Yang, and R. G. Parr, Phys. Rev. B **37**, 785 (1988).

[18] J. P. Perdew, A. Ruzsinszky, G. I. Csonka, L. A. Constantin, and J. Sun, Phys. Rev. Lett. **103**, 026403 (2009).

[19] J. Tao, J. P. Perdew, V. N. Staroverov, and G. E. Scuseria, Phys. Rev. Lett. **91**, 146401 (2003).

[20] J. Tao and Y. Mo, Phys. Rev. Lett. **117**, 073001 (2016).

[21] B. Patra, S. Jana, L. A. Constantin, and P. Samal, Phys. Rev. B **100**, 155140 (2019).

[22] L. A. Constantin, E. Fabiano, J. M. Pitarke, and F. Della Sala, Phys. Rev. B **93**, 115127 (2016).

[23] L. A. Constantin, E. Fabiano, and F. Della Sala, J. Chem. Phys. **145**, 084110 (2016).

[24] L. A. Constantin, A. Terentjevs, F. Della Sala, and E. Fabiano, Phys. Rev. B **91**, 041120(R) (2015).

[25] L. A. Constantin, L. Chiodo, E. Fabiano, I. Bodrenko, and F. D. Sala, Phys. Rev. B **84**, 045126 (2011).

[26] J. Sun, A. Ruzsinszky, and J. P. Perdew, Phys. Rev. Lett. **115**, 036402 (2015).

[27] J. W. Furness, A. D. Kaplan, J. Ning, J. P. Perdew, and J. Sun, J. Phys. Chem. Lett. **11**, 8208 (2020).

[28] D. Mejía-Rodríguez and S. B. Trickey, Phys. Rev. B **102**, 121109(R) (2020).

[29] S. Jana, S. K. Behera, S. Śmiga, L. A. Constantin, and P. Samal, New J. Phys. **23**, 063007 (2021).

[30] S. Jana, K. Sharma, and P. Samal, J. Phys. Chem. A **123**, 6356 (2019).

[31] A. Patra, S. Jana, and P. Samal, J. Chem. Phys. **153**, 184112 (2020).

[32] S. Jana, S. K. Behera, S. Śmiga, L. A. Constantin, and P. Samal, J. Chem. Phys. **155**, 024103 (2021).

[33] N. E. Singh-Miller and N. Marzari, Phys. Rev. B **80**, 235407 (2009).

[34] A. Patra, J. E. Bates, J. Sun, and J. P. Perdew, Proc. Natl. Acad. Sci. USA, **114**, E9188 (2017).

[35] S. Jana, A. Patra, and P. Samal, J. Chem. Phys. **149**, 044120 (2018).

[36] P. Haas, F. Tran, and P. Blaha, Phys. Rev. B **79**, 085104 (2009).

[37] J. Sun, M. Marsman, G. I. Csonka, A. Ruzsinszky, P. Hao, Y.-S. Kim, G. Kresse, and J. P. Perdew, Phys. Rev. B **84**, 035117 (2011).

[38] F. Tran, J. Stelzl, and P. Blaha, J. Chem. Phys. **144**, 204120 (2016).

[39] Y. Mo, R. Car, V. N. Staroverov, G. E. Scuseria, and J. Tao, Phys. Rev. B **95**, 035118 (2017).

[40] H. Peng and J. P. Perdew, Phys. Rev. B **96**, 100101(R) (2017).

[41] Y. Zhang, J. Sun, J. P. Perdew, and X. Wu, Phys. Rev. B **96**, 035143 (2017).

[42] C. Shahi, J. Sun, and J. P. Perdew, Phys. Rev. B **97**, 094111 (2018).

[43] S. Jana, K. Sharma, and P. Samal, J. Chem. Phys. **149**, 164703 (2018).

[44] B. Patra, S. Jana, L. A. Constantin, and P. Samal, J. Phys. Chem. C **125**, 4284 (2021).

[45] S. Jana, A. Patra, S. Śmiga, L. A. Constantin, and P. Samal, J. Chem. Phys. **153**, 214116 (2020).

[46] A. Ghosh, S. Jana, M. K. Niranjan, S. K. Behera, L. A. Constantin, and P. Samal, J. Phys.: Condens. Matter **34**, 075501 (2022).

[47] J. P. Perdew, W. Yang, K. Burke, Z. Yang, E. K. U. Gross, M. Scheffler, G. E. Scuseria, T. M. Henderson, I. Y. Zhang, A. Ruzsinszky, H. Peng, J. Sun, E. Trushin, and A. Görling, Proc. Natl. Acad. Sci. USA **114**, 2801 (2017).

[48] F. Tran, P. Blaha, and K. Schwarz, J. Phys.: Condens. Matter **19**, 196208 (2007).

[49] P. Borlido, J. Schmidt, A. W. Huran, F. Tran, M. A. L. Marques, and S. Botti, npj Comput. Mater. **6**, 96 (2020).

[50] B. Patra, S. Jana, L. A. Constantin, and P. Samal, Phys. Rev. B **100**, 045147 (2019).

[51] F. Tran, S. Ehsan, and P. Blaha, Phys. Rev. Mater. **2**, 023802 (2018).

[52] F. Tran and P. Blaha, J. Phys. Chem. A **121**, 3318 (2017).

[53] F. Tran, J. Doumont, L. Kalantari, A. W. Huran, M. A. L. Marques, and P. Blaha, J. Appl. Phys. **126**, 110902 (2019).

[54] J. Paier, M. Marsman, and G. Kresse, Phys. Rev. B **78**, 121201(R) (2008).

[55] D. Wing, J. B. Haber, R. Noff, B. Barker, D. A. Egger, A. Ramasubramaniam, S. G. Louie, J. B. Neaton, and L. Kronik, Phys. Rev. Mater. **3**, 064603 (2019).

[56] M. Städele, M. Moukara, J. A. Majewski, P. Vogl, and A. Görling, Phys. Rev. B **59**, 10031 (1999).

[57] M. Petersilka, U. J. Gossmann, and E. K. U. Gross, Phys. Rev. Lett. **76**, 1212 (1996).

[58] Y.-H. Kim and A. Görling, Phys. Rev. Lett. **89**, 096402 (2002).

[59] A. V. Terentjev, L. A. Constantin, and J. M. Pitarke, Phys. Rev. B **98**, 085123 (2018).

[60] S. Sharma, J. K. Dewhurst, A. Sanna, and E. K. U. Gross, Phys. Rev. Lett. **107**, 186401 (2011).

[61] S. Rigamonti, S. Botti, V. Veniard, C. Draxl, L. Reining, and F. Sottile, Phys. Rev. Lett. **114**, 146402 (2015).

[62] M. van Faassen, P. L. de Boeij, R. van Leeuwen, J. A. Berger, and J. G. Snijders, Phys. Rev. Lett. **88**, 186401 (2002).

[63] S. Cavo, J. A. Berger, and P. Romaniello, Phys. Rev. B **101**, 115109 (2020).

[64] S. Jana, B. Patra, S. Śmiga, L. A. Constantin, and P. Samal, Phys. Rev. B **102**, 155107 (2020).

[65] G. Ohad, D. Wing, S. E. Gant, A. V. Cohen, J. B. Haber, F. Sagredo, M. R. Filip, J. B. Neaton, and L. Kronik, Phys. Rev. Mater. **6**, 104606 (2022).

[66] A. Ramasubramaniam, D. Wing, and L. Kronik, Phys. Rev. Mater. **3**, 084007 (2019).

[67] P. Deák, M. Lorke, B. Aradi, and T. Frauenheim, J. Appl. Phys. **126**, 130901 (2019).

[68] D. K. Lewis, M. Matsubara, E. Bellotti, and S. Sharifzadeh, Phys. Rev. B **96**, 235203 (2017).

[69] E. R. Batista, J. Heyd, R. G. Hennig, B. P. Uberuaga, R. L. Martin, G. E. Scuseria, C. J. Umrigar, and J. W. Wilkins, Phys. Rev. B **74**, 121102(R) (2006).

[70] P. Deák, B. Aradi, T. Frauenheim, E. Janzén, and A. Gali, Phys. Rev. B **81**, 153203 (2010).

[71] T. Rauch, F. Munoz, M. A. L. Marques, and S. Botti, Phys. Rev. B **104**, 064105 (2021).

[72] Y. Shu and D. G. Truhlar, J. Chem. Theory Comput. **16**, 4337 (2020).

[73] J. Heyd, G. E. Scuseria, and M. Ernzerhof, J. Chem. Phys. **118**, 8207 (2003).

[74] A. V. Krukau, O. A. Vydrov, A. F. Izmaylov, and G. E. Scuseria, J. Chem. Phys. **125**, 224106 (2006).

[75] J. Tao, V. N. Staroverov, G. E. Scuseria, and J. P. Perdew, Phys. Rev. A **77**, 012509 (2008).

[76] J. Heyd and G. E. Scuseria, J. Chem. Phys. **121**, 1187 (2004).

[77] S. Jana, A. Patra, L. A. Constantin, and P. Samal, J. Chem. Phys. **152**, 044111 (2020).

[78] S. Jana, L. A. Constantin, S. Śmiga, and P. Samal, J. Chem. Phys. **157**, 024102 (2022).

[79] S. Jana and P. Samal, Phys. Chem. Chem. Phys. **20**, 8999 (2018).

[80] B. Patra, S. Jana, and P. Samal, Phys. Chem. Chem. Phys. **20**, 8991 (2018).

[81] S. Jana, A. Patra, L. A. Constantin, H. Myneni, and P. Samal, Phys. Rev. A **99**, 042515 (2019).

[82] S. Jana and P. Samal, Phys. Chem. Chem. Phys. **21**, 3002 (2019).

[83] S. Jana, B. Patra, H. Myneni, and P. Samal, Chem. Phys. Lett. **713**, 1 (2018).

[84] R. Garrick, A. Natan, T. Gould, and L. Kronik, Phys. Rev. X **10**, 021040 (2020).

[85] X. Wang, M. Dvorak, and Z. Wu, Phys. Rev. B **94**, 195429 (2016).

[86] T. Shimazaki and T. Nakajima, J. Chem. Phys. **141**, 114109 (2014).

[87] J. H. Skone, M. Govoni, and G. Galli, Phys. Rev. B **89**, 195112 (2014).

[88] N. P. Brawand, M. Vörös, M. Govoni, and G. Galli, Phys. Rev. X **6**, 041002 (2016).

[89] J. H. Skone, M. Govoni, and G. Galli, Phys. Rev. B **93**, 235106 (2016).

[90] W. Chen, G. Miceli, G.-M. Rignanese, and A. Pasquarello, Phys. Rev. Mater. **2**, 073803 (2018).

[91] Z.-H. Cui, Y.-C. Wang, M.-Y. Zhang, X. Xu, and H. Jiang, J. Phys. Chem. Lett. **9**, 2338 (2018).

[92] M. Lorke, P. Deák, and T. Frauenheim, Phys. Rev. B **102**, 235168 (2020).

[93] M. Gerosa, C. E. Bottani, L. Caramella, G. Onida, C. Di Valentin, and G. Pacchioni, J. Chem. Phys. **143**, 134702 (2015).

[94] M. Gerosa, C. E. Bottani, L. Caramella, G. Onida, C. Di Valentin, and G. Pacchioni, Phys. Rev. B **91**, 155201 (2015).

[95] G. Miceli, W. Chen, I. Reshetnyak, and A. Pasquarello, Phys. Rev. B **97**, 121112(R) (2018).

[96] H. Zheng, M. Govoni, and G. Galli, Phys. Rev. Mater. **3**, 073803 (2019).

[97] M. Gerosa, C. E. Bottani, C. D. Valentin, G. Onida, and G. Pacchioni, J. Phys.: Condens. Matter **30**, 044003 (2018).

[98] Y. Hinuma, Y. Kumagai, I. Tanaka, and F. Oba, Phys. Rev. B **95**, 075302 (2017).

[99] N. P. Brawand, M. Govoni, M. Vörös, and G. Galli, J. Chem. Theory Comput. **13**, 3318 (2017).

[100] P. Liu, C. Franchini, M. Marsman, and G. Kresse, J. Phys.: Condens. Matter **32**, 015502 (2020).

[101] A. Grüneis, G. Kresse, Y. Hinuma, and F. Oba, Phys. Rev. Lett. **112**, 096401 (2014).

[102] L. Kronik and S. Kümmel, Adv. Mater. **30**, 1706560 (2018).

[103] O. A. Vydrov and G. E. Scuseria, J. Chem. Phys. **125**, 234109 (2006).

[104] L. Kronik, T. Stein, S. Refaely-Abramson, and R. Baer, J. Chem. Theory Comput. **8**, 1515 (2012).

[105] M. Ernzerhof and G. E. Scuseria, J. Chem. Phys. **110**, 5029 (1999).

[106] I. Souza, J. Íñiguez, and D. Vanderbilt, Phys. Rev. Lett. **89**, 117602 (2002).

[107] R. W. Nunes and X. Gonze, Phys. Rev. B **63**, 155107 (2001).

[108] M. Gajdoš, K. Hummer, G. Kresse, J. Furthmüller, and F. Bechstedt, Phys. Rev. B **73**, 045112 (2006).

[109] T. Olsen, C. E. Patrick, J. E. Bates, A. Ruzsinszky, and K. S. Thygesen, npj Comput. Mater. **5**, 106 (2019).

[110] H. F. Wilson, F. Gygi, and G. Galli, Phys. Rev. B **78**, 113303 (2008).

[111] E. K. U. Gross, J. F. Dobson, and M. Petersilka, in *Density Functional Theory II: Relativistic and Time Dependent Extensions*, edited by R. F. Nalewajski (Springer, Berlin, 1996), pp. 81–172.

[112] J. Harris and A. Griffin, Phys. Rev. B **11**, 3669 (1975).

[113] D. C. Langreth and J. P. Perdew, Phys. Rev. B **15**, 2884 (1977).

[114] L. A. Constantin and J. M. Pitarke, Phys. Rev. B **75**, 245127 (2007).

[115] L. A. Constantin, Phys. Rev. B **93**, 121104(R) (2016).

[116] S. Ichimaru, Rev. Mod. Phys. **54**, 1017 (1982).

[117] J. P. Perdew and Y. Wang, Phys. Rev. B **45**, 13244 (1992).

[118] J. P. Perdew, D. C. Langreth, and V. Sahni, Phys. Rev. Lett. **38**, 1030 (1977).

[119] S. Moroni, D. M. Ceperley, and G. Senatore, Phys. Rev. Lett. **75**, 689 (1995).

[120] F. Tran and P. Blaha, Phys. Rev. Lett. **102**, 226401 (2009).

[121] T. c. v. Rauch, M. A. L. Marques, and S. Botti, Phys. Rev. B **101**, 245163 (2020).

[122] T. Rauch, M. A. L. Marques, and S. Botti, J. Chem. Theory Comput. **16**, 2654 (2020).

[123] F. Tran, J. Doumont, L. Kalantari, P. Blaha, T. Rauch, P. Borlido, S. Botti, M. A. L. Marques, A. Patra, S. Jana, and P. Samal, J. Chem. Phys. **155**, 104103 (2021).

[124] A. Patra, S. Jana, P. Samal, F. Tran, L. Kalantari, J. Doumont, and P. Blaha, J. Phys. Chem. C **125**, 11206 (2021).

[125] M. A. L. Marques, J. Vidal, M. J. T. Oliveira, L. Reining, and S. Botti, Phys. Rev. B **83**, 035119 (2011).

[126] A. V. Krukau, G. E. Scuseria, J. P. Perdew, and A. Savin, J. Chem. Phys. **129**, 124103 (2008).

[127] Computer code ELK, https://elk.sourceforge.io/

[128] D. J. Singh, *Planewaves, Pseudopotentials and the LAPW Method* (Springer, New York, NY, 2013).

[129] G. Kresse and J. Hafner, Phys. Rev. B **47**, 558 (1993).

[130] G. Kresse and J. Furthmüller, Phys. Rev. B **54**, 11169 (1996).

[131] G. Kresse and D. Joubert, Phys. Rev. B **59**, 1758 (1999).

[132] G. Kresse and J. Furthmüller, Comput. Mater. Sci. **6**, 15 (1996).

[133] H. Jiang and Y.-C. Shen, J. Chem. Phys. **139**, 164114 (2013).

[134] H. Jiang and P. Blaha, Phys. Rev. B **93**, 115203 (2016).

[135] Y. Hinuma, A. Grüneis, G. Kresse, and F. Oba, Phys. Rev. B **90**, 155405 (2014).

[136] A. Ghosh, S. Jana, T. Rauch, F. Tran, M. A. L. Marques, S. Botti, L. A. Constantin, M. K. Niranjan, and P. Samal, J. Chem. Phys. **157**, 124108 (2022).

[137] LOCPOT, Vaspwiki, VASP, https://www.vasp.at/wiki/index.php/LOCPOT.

[138] T. Stein, H. Eisenberg, L. Kronik, and R. Baer, Phys. Rev. Lett. **105**, 266802 (2010).

[139] N. L. Nguyen, N. Colonna, A. Ferretti, and N. Marzari, Phys. Rev. X **8**, 021051 (2018).

[140] H.-G. Birken, C. Blessing, and C. Kunz, in *Handbook of Optical Constants of Solids*, edited by E. D. Palik (Academic Press, Boston, 1998), pp. 279–292.

[141] S. Logothetidis, P. Lautenschlager, and M. Cardona, Phys. Rev. B **33**, 1110 (1986).

[142] D. M. Roessler and W. C. Walker, Phys. Rev. **166**, 599 (1968).

[143] M. L. Bortz, R. H. French, D. J. Jones, R. V. Kasowski, and F. S. Ohuchi, Phys. Scr. **41**, 537 (1990).

[144] A. Tal, P. Liu, G. Kresse, and A. Pasquarello, Phys. Rev. Res. **2**, 032019(R) (2020).

[145] F. Kootstra, P. L. de Boeij, and J. G. Snijders, Phys. Rev. B **62**, 7071 (2000).

[146] D. M. Roessler and W. C. Walker, Phys. Rev. **159**, 733 (1967).

[147] C. A. Ullrich, *Time-Dependent Density-Functional Theory: Concepts and Applications* (Oxford University Press, Oxford, 2011).

[148] Z.-h. Yang, F. Sottile, and C. A. Ullrich, Phys. Rev. B **92**, 035202 (2015).

[149] J. Sun and C. A. Ullrich, Phys. Rev. Mater. **4**, 095402 (2020).

[150] J. Sun, J. Yang, and C. A. Ullrich, Phys. Rev. Res. **2**, 013091 (2020).

[151] P. E. Trevisanutto, A. Terentjevs, L. A. Constantin, V. Olevano, and F. D. Sala, Phys. Rev. B **87**, 205143 (2013).

[152] Y.-M. Byun and C. A. Ullrich, Phys. Rev. B **95**, 205136 (2017).

[153] Y.-M. Byun, J. Sun, and C. A. Ullrich, Electron. Struct. **2**, 023002 (2020).

[154] Improving the dielectric function, Vaspwiki, VASP, https://www.vasp.at/wiki/index.php/Improving_the_dielectric_function.

[155] S. Baroni, S. de Gironcoli, A. Dal Corso, and P. Giannozzi, Rev. Mod. Phys. **73**, 515 (2001).

[156] X. Gonze and C. Lee, Phys. Rev. B **55**, 10355 (1997).